THE ASTROPHYSICAL JOURNAL, 453:293–307, 1995 November 1


# STUDY OF STRUCTURE AND SMALL-SCALE FRAGMENTATION IN TMC-1

W. D. LANGER, T. VELUSAMY,[1] T. B. H. KUIPER, S. LEVIN, AND E. OLSEN
Jet Propulsion Laboratory, California Institute of Technology, MS 169-506, Pasadena, CA 91109

AND

V. MIGENES
Australia National Telescope Facility, CSIRO, PO Box 76, Epping, NSW 2121 Australia
*Received 1993 September 1; accepted 1995 May 11*

## ABSTRACT

Large-scale $C^{18}O$ maps show that the Taurus molecular cloud 1 (TMC-1) has numerous cores located along a ridge which extends about 12′ by at least 35′. The cores traced by $C^{18}O$ are about a few arcminutes (0.1–0.2 pc) in extent, typically contain about 0.5–3 $M_\odot$, and are probably gravitationally bound. We present a detailed study of the small-scale fragmentary structure of one of these cores, called core D, within TMC-1 using very high spectral and spatial resolution maps of CCS and CS. The CCS lines are excellent tracers for investigating the density, temperature, and velocity structure in dense cores. The high spectral resolution, 0.008 km $s^{-1}$, data consist mainly of single-dish, Nyquist-sampled maps of CCS at 22 GHz with 45″ spatial resolution taken with NASA's 70 m DSN antenna at Goldstone. The high spatial resolution spectral line maps were made with the Very Large Array (9″ resolution) at 22 GHz and with the OVRO millimeter array in CCS and CS at 93 GHz and 98 GHz, respectively, with 6″ resolution. These maps are supplemented with single-dish observations of CCS and $CC^{34}S$ spectra at 33 GHz using a NASA 34 m DSN antenna, CCS 93 GHz, $C^{34}S$ (2–1), and $C^{18}O$ (1–0) single-dish observations made with the AT&T Bell Laboratories 7 m antenna.

Our high spectral and spatial CCS and CS maps show that core D is highly fragmented. The single-dish CCS observations map out several clumps which range in size from ∼45″ to 90″ (0.03–0.06 pc). These clumps have very narrow intrinsic line widths, 0.11–0.25 km $s^{-1}$, slightly larger than the thermal line width for CCS at 10 K, and masses about 0.03–0.2 $M_\odot$. Interferometer observations of some of these clumps show that they have considerable additional internal structure, consisting of several condensations ranging in size from ∼10″–30″ (0.007–0.021 pc), also with narrow line widths. The mass of these smallest fragments is of order 0.01 $M_\odot$. These small-scale structures traced by CCS appear to be gravitationally unbound by a large factor. Most of these objects have masses that fall below those of the putative proto–brown dwarfs ($\lesssim$0.1 $M_\odot$). The presence of many small gravitationally unbound clumps suggests that fragmentation mechanisms other than a purely Jeans gravitational instability may be important for the dynamics of these cold dense cores.

*Subject headings:* ISM: clouds — ISM: individual (Taurus molecular cloud) — ISM: molecules — stars: formation — radio lines: ISM

## 1. INTRODUCTION

The overall structure of molecular clouds is self-similar over a range of masses which is at least 1–1000 $M_\odot$ (Falgarone, Phillips, & Walker 1991). The observed Larson (1981) power-law relationship between the spectral line width and the size of clouds, $\Delta V$ (km $s^{-1}$) $\propto R(\mathrm{pc})^{0.5}$, strongly suggests that macro-turbulent (supersonic) motions govern the structure of these clouds at larger scale (Miesch & Bally 1994). Under these conditions $\Delta V_{\mathrm{turb}} \gg \Delta V_{\mathrm{thermal}}$, where $\Delta V_{\mathrm{thermal}} \simeq 0.5$–$1.0$ km $s^{-1}$ is the order of the sound speed of molecular hydrogen under typical interstellar cloud conditions. Throughout this range in $\Delta V$, the relationship between mass, line width, and size is roughly consistent with the virial theorem (Myers et al. 1991; Tatematsu et al. 1993), which is to say that gravitational and pressure forces are comparable.

In the cores of cold dense clouds, a different set of conditions prevails, since there are many examples of line widths measured with trace molecules, CO, CS, $NH_3$, and $HC_3N$, that are narrower than the thermal line width of molecular hydrogen at 10 K. In these cases the velocity field is mainly thermal and has a small nonthermal component, which is probably a result of microturbulent (subsonic) motions but could have contributions from systematic motion (rotation and infall). In the cores where $\Delta V_{\mathrm{turb}} < \Delta V_{\mathrm{thermal}}$, their support is mainly thermal pressure.

In a turbulent medium, the smallest scale in the self-similarity occurs where dissipation becomes the dominant process. Extrapolating the Larson velocity-size relationship to the point where the velocity dispersion equals the thermal line width of molecular hydrogen yields a scale of about 0.15 pc, or a typical size of a "Myers" core. While there is no a priori reason why the Larson scaling law should be valid in this regime, the results of Fuller & Myers (1993) seem to indicate that this relationship can be extended down to much narrower lines and smaller regions about 0.02–0.03 pc (4200–6200 AU). Indeed, Kitamura et al. (1993) have suggested that most of the turbulent energy in the nearby quiescent Taurus molecular cloud-1C (TMC-1C) is at about this scale, 0.03 pc.

These observations of small-scale thermal features raise some important questions regarding the structure and velocity dispersion in cold cores. What are the mechanisms for fragmentation and formation of protostars? How is turbulence generated and dissipated, and how does the transition from

[1] Also Tata Institute of Fundamental Research, Bombay, India.

macro- to microturbulence, and finally to purely thermal velocity dispersion, take place? What decides the final state leading to, and the mass of, a protostar? Furthermore, a search for small, low-mass structures bears on the question of the low-mass cutoff of the initial mass function (IMF) and whether there are proto–brown dwarfs with mass $<0.08\ M_\odot$. To address these issues, we need extensive observations of the physical conditions in cloud cores over a large range of spatial scales.

In the classical Hoyle (1953) picture of protostar formation, hierarchical gravitational fragmentation takes place by Jeans's instability until a small enough mass is reached whereby further fragmentation halts (see Spitzer 1968). One problem with this model is that the fragments do not separate out in purely spherical collapse (see Monaghan & Lattanzio 1991). This model also does not explain the Larson relation between size and velocity dispersion, or the number of clumps as a function of size in interstellar clouds (see Williams, de Geus, & Blitz 1994). To resolve this problem, Henriksen & Turner (1984) have proposed that the Larsen relationship arises from the scaling of a compressible turbulent fluid driven by gravity and outward transport of angular momentum. In contrast to such dynamical models, steady state models based on a balance between gravitational fragmentation of large clumps and coalescence of small ones (Nakano 1984) purport to explain the mass spectrum of fragments observed in large molecular cloud structures (see Williams et al. 1994). However, it is not obvious that such models apply to the colder, less massive clouds or cloud complexes, such as the Taurus molecular cloud complex. Murray et al. (1993) have suggested that fragmentation by thermal instabilities and coalescence of fragments are important mechanisms in the formation of galaxies, star clusters, and individual stars. While such thermal instabilities arise readily in the diffuse ISM, where different coolants in high- and low-density atomic gas can maintain a large contrast in temperature, it is not obvious that such states can be achieved in molecular gas, where the temperature contrast is low in different gas densities. In general, we lack observational information to test or discriminate among such clouds.

Nearby cloud complexes afford us an excellent opportunity to study models of cloud evolution, fragmentation, and protostar formation. Ground-breaking work on nearby cloud cores was done by Myers and his associates (e.g., Myers & Benson 1983; Benson & Myers 1989; Myers et al. 1991; Fuller & Myers 1992; Myers & Fuller 1992; Fuller & Myers 1993; Goodman et al. 1993). However, to study the small-scale structures within the dense cores we need to measure the density, temperature, chemical composition, and velocity field with a spatial and spectral resolution smaller than the scale of the structures of interest. Such studies of structure and chemical composition of these cores in nearby clouds requires spatial resolution from 5″ to 45″ appropriate for a wide range of scale sizes and a spectral resolution $\leq 0.03$ km s$^{-1}$ necessary to resolve thermal widths of blended velocity components.

One of the best-studied regions of fragmentation and protostar formation is the dark cloud TMC-1 in Taurus. It has been mapped at moderate resolution, 5′, in $^{13}CO$, $C^{18}O$, and $HCO^+$ (Duvert, Cernicharo, & Baudry 1986), at $\sim 2'$ in $H^{13}CO^+$ (Guélin, Langer, & Wilson 1982), CS (Snell, Langer, & Frerking 1982), $HC_3N$, and $NH_3$ (Tölle et al. 1981), and at higher spatial resolution $\sim 45''$ in $HC_7N$ (Olano, Walmsley, & Wilson 1988). All these maps show that TMC-1 has several moderate-size cores about 3′ in diameter. Six cores were identified in the spatial velocity CS maps (Snell et al. 1982) and CCS maps (Hirahara et al. 1992). These Myers cores (see Myers et al. 1991) with size $\sim 0.16$ pc (3′–4′ in diameter at the distance to TMC) have typical masses $\sim 1$–$2\ M_\odot$ assuming an average density $\sim 10^4$ cm$^{-3}$ as suggested by CS observations (Snell et al. 1982).

However, our understanding of the smaller scale structures in TMC-1 (see Hirahara et al. 1992) has been limited by the paucity of high spatial resolution observations and also the confusion that arises from the complex velocity field in this region as indicated by the line shapes of various tracers (see $HC_3N$ spectra by Tölle et al. 1981). Here we extend the study of the features in TMC-1 to small scale about 6″ by mapping of one of its cores, called core D by Hirahara et al. (1992) and fragment-C by Snell et al. (1982), in CCS and CS.

The carbon chain molecule CCS is widespread in dark clouds (Fuente et al. 1990; Suzuki et al. 1992). CCS lines are excellent tracers for investigating the velocity structure in dense cores because they have no hyperfine structure, have an intrinsically narrow thermal line width (0.09 km s$^{-1}$ at 10 K), require high density for excitation and, as we show, are not very opaque in TMC-1. Their intrinsic narrow thermal line widths afford better separation of velocity structure of individual components than less massive molecules such as CO and $NH_3$. In addition, CCS has many accessible transitions at centimeter and millimeter frequencies that make it a good density probe over the range $10^4$–$10^6$ cm$^{-3}$ for the low kinetic temperatures present in dense cold cores. All these properties make CCS a potentially good tracer to search for small-scale structures within the cold cloud cores.

We mapped TMC-1 core D extensively in CCS at 22.3 GHz with very high velocity resolution of 0.008 km s$^{-1}$. Our motivation for using such high spectral resolution was that if the quiescent cloud cores contained several small features, then it might be possible to count and separate them by resolving them spectrally rather than spatially (Velusamy et al. 1993). We also observed CCS and $CC^{34}S$ at 33.75 and 33.1 GHz, respectively, at the central position to determine whether CCS is optically thick or self-absorbed, and the CCS transition at 93 GHz to obtain excitation information about CCS. From the larger maps of CCS made with the single-dish antennas we selected a few fields for observation at very high spatial resolution using the following interferometers: CCS 22 GHz at the Very Large Array (VLA),[2] CCS 93 GHz and CS 98 GHz observations at the OVRO-millimeter array (MMA). To get an overall view of the dense regions of TMC-1 we also made a large-scale map of $C^{18}O$ ($J = 1$–0) emission with the AT&T Bell Laboratories 7 m antenna. Our analysis of these data indicates that TMC-1 is highly fragmented with structures ranging in size from 10″ to 10′. The mass of the smaller clumps mapped with CCS range from about 0.01 to 0.15 $M_\odot$. The larger features traced by $C^{18}O$ range in mass from 0.5 to 30 $M_\odot$. Most of the larger structures, as seen in $C^{18}O$, are gravitationally bound while most of the smallest structures, as seen in CCS and CS, are unbound. The presence of so many unbound features with low mass raises important questions about their formation, lifetime, and relationship to the protostar formation process, and origin of the initial mass function.

[2] The VLA is a facility of the National Radio Astronomy Observatory, which is operated by Associated Universities Inc., under contract with the National Science Foundation.

## 2. OBSERVATIONS

The transitions observed and the telescopes used are described in Table 1. The CCS ($J_N = 2_1$–$1_0$) line rest frequency, 22.344033 GHz, is taken from Saito et al. (1987). The frequencies of the CCS and $CC^{34}S$ ($J_N = 3_2$–$2_1$) and CCS ($J_N = 8_7$–$7_6$) transitions were taken from the JPL Spectral Line Catalog (Pickett, Poynter, & Cohen 1991). Note that we have adopted the notation of Saito et al. for labeling the levels with ($N$, $J$). The JPL catalog assigns a different labeling of ($N$, $J$) whereby the $N$ quantum number is assigned to the state of a given $J$ which has the largest contribution from the basis function with the same $N$ quantum number (Pickett et al. 1991). The frequency of the $J = 20 \rightarrow 19$ transition of $HC_7N$ was calculated from constants given by Kroto et al. (1978).

TMC-1 was mapped over a 30′ by 30′ region in $C^{18}O$ ($J = 1 \rightarrow 0$) using the AT&T Bell Laboratories 7 m antenna in 1993 and 1994. The FWHM beamwidth of the antenna is 100″ at 110 GHz, and our map was sampled every 60″, or almost at the Nyquist sampling. The spectral resolution was 50 kHz, corresponding to 0.14 km s$^{-1}$ velocity resolution. The receiver, calibration, and observing procedures are discussed in Langer, Glassgold, & Wilson (1987).

We mapped one of the cores in TMC-1 (core-D in the CCS map of Hirahara et al. 1992) in the CCS 22 GHz transition with high signal-to-noise ratio, Nyquist sampling every 24″ over 4′ × 4′ region around the peak. The map was centered at R.A.(1950) = $04^h38^m42^s.0$; decl.(1950) = 25°34′50″. The observations were made between 1993 March 13 and 1994 April 1, using NASA's Deep Space Network (DSN) 70 m antenna at Goldstone, California. At 22 GHz, the antenna HPBW is 45″ and the pointing accuracy was better than 7″. We measured the main beam efficiency to be 42% for point sources and about 70% for the extended source structure of TMC-1, as determined from beam shape and observations of the Moon. The receiver consisted of a maser preamplifier followed by a digitally controlled Hewlett-Packard downconverter with a synthesized local oscillator locked to the station hydrogen maser frequency standard. The system has a noise temperature of ~60 K measured at the zenith. We used the two million channel Wide Band Spectrum Analyzer (Quirk et al. 1988) with a spectral resolution of 19 Hz over 40 MHz. The resolution was reduced by co-adding 32 adjacent channels to provide 8192 channels of 610 Hz resolution (or 0.008 km s$^{-1}$ at 22 GHz). The spectra were observed in position switching mode and were Doppler corrected to an accuracy of 0.004 km s$^{-1}$, using the NRAO "dopset" routine.

The 33 GHz spectral line observations were made using the same spectrometer and the 34 m beam waveguide antenna of the research and development station (DSS-13) at Goldstone with an HPBW of 70″. The receiver consisted of a cryogenically cooled HEMT preamplifier followed by a two-stage downconverter which is part of the station's core equipment. The downconverter local oscillators are locked to the hydrogen maser. The CCS 93 and $C^{34}S$ 96 GHz lines were observed with the AT&T Bell Laboratories 7 m antenna in 1993–1994 using 12.5 kHz spectral resolution. The antenna HPBW is 120″, and the aperture efficiency is greater than 90%. The receiver, calibration, and observing procedures are similar to those discussed in Langer et al. (1987).

The VLA CCS spectral line maps at 22 GHz were made in D-configuration on 1994 January 4 and 6 for 7 hr total, with velocity resolution ~0.04 km s$^{-1}$. The data were taken using 256 channels and 0.78 MHz bandwidth without Hanning smoothing. The source 0528+134 was used for amplitude and phase calibration and also for passband calibration. The flux density of the calibrator was 6.14 Jy at 22 GHz. The spectral line maps were produced using AIPS. In order to maximize the signal-to-noise ratio in the maps, they were smoothed to a lower resolution of 9″.

The CCS and CS OVRO-MMA spectral line maps were made between 1993 October and 1994 November. Our initial observations (1993–1994 observing season) used the five antenna array with the map center at R.A.(1950) = $04^h38^m42^s.0$ and decl.(1950) = 25°34′50″. Both the CCS and CS spectra were detected in the shortest baseline (15 m), and their maps showed that the peak emission was located away from this map center. In our second set of observations in 1994 October–November we used new map centers: CCS was observed at the emission peak in the VLA map [R.A.(1950) = $04^h38^m42^s.3$ and decl.(1950) = 25°35′25″], and CS was observed at emission peak seen in the earlier (1993–1994) observations [R.A.(1950) = $04^h38^m43^s.5$ and decl.(1950) = 25°34′50″]. The results presented here are from this second set of observations and used the six antennas in configuration A. The data were taken using 128 channels with 1.98 MHz bandwidth without on-line Hanning smoothing. Source 0528+134 was used for both amplitude and phase calibration. The flux density of the calibrator was 4.9 and 5.2 Jy at 93 and 98 GHz, respectively. The radio sources 3C 273 and 3C 454.3 were used for passband calibration of the spectral line data. The data were calibrated using the Owens Valley millimeter array software, and the spectral line maps were produced using AIPS. In the case of

TABLE 1

SPECTRAL LINE FREQUENCIES AND TELESCOPES

| Molecule | Transition | Frequency (GHz) | Antenna | HPBW | Velocity Resolution (km s$^{-1}$) | Spatial Resolution[a] (pc) |
|---|---|---|---|---|---|---|
| CCS ..... | $J_N = 2_1 \rightarrow 1_0$ | 22.344033 | DSN 70 m | 45″ | 0.008 | 0.030 |
| | $J_N = 2_1 \rightarrow 1_0$ | 22.344033 | VLA-D | 9 | 0.041 | 0.006 |
| | $J_N = 3_2 \rightarrow 2_1$ | 33.751374 | DSN 34 m | 70 | 0.011 | 0.048 |
| | $J_N = 8_7 \rightarrow 7_6$ | 93.870107 | AT&T 7 m | 120 | 0.040 | 0.080 |
| | $J = 8_7 \rightarrow 7_6$ | 93.870107 | OVRO-MMA | 9 | 0.052 | 0.006 |
| $HC_7N$ ..... | $J = 20 \rightarrow 19$ | 22.559907 | DSN 70 m | 45 | 0.050 | 0.030 |
| $CC^{34}S$ ..... | $J_N = 3_2 \rightarrow 2_1$ | 33.111839 | DSN 34 m | 70 | 0.011 | 0.048 |
| CS ..... | $J = 2 \rightarrow 1$ | 97.90968 | OVRO-MMA | 6 | 0.049 | 0.004 |
| $C^{34}S$ ..... | $J = 2 \rightarrow 1$ | 96.412953 | AT&T 7 m | 115 | 0.039 | 0.078 |
| $C^{18}O$ ..... | $J = 1 \rightarrow 0$ | 109.782182 | AT&T 7 m | 100 | 0.140 | 0.068 |

[a] Spatial resolution calculated at the distance to TMC-1, 140 pc.

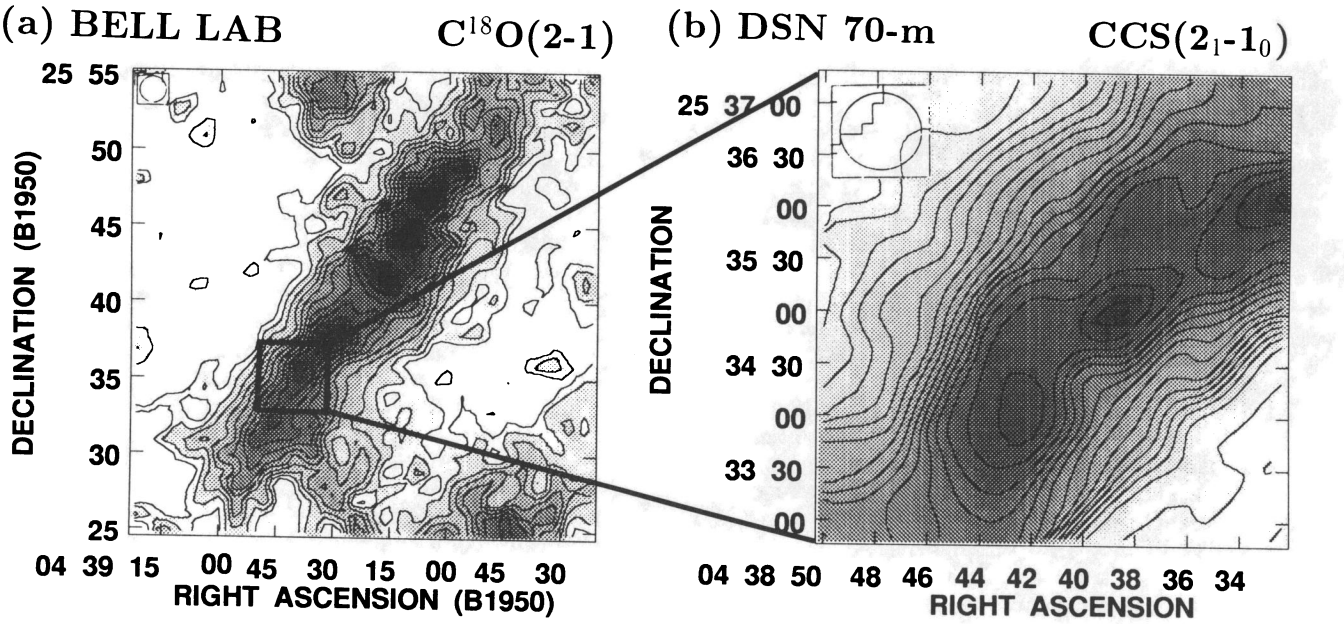


FIG. 1.—(*a*) $C^{18}O$ (1–0) integrated intensity map of TMC-1 from the AT&T Bell Laboratories 7 m antenna: 1′ sampling; 1.′7 beam size. The lowest contour and the contour interval are 0.4 and 0.2 km $s^{-1}$, respectively. The box represents the region containing core D centered at R.A.(1950) = $04^h38^m42^s.0$, decl.(1950) = 25°34′50″. (*b*) CCS 22 GHz total integrated intensity map of core D over a 4′ by 4′ region. These data are taken with the DSN 70 m antenna, which has an angular resolution of 45″; the map is Nyquist sampled every 24″. The first contour and contour interval are 0.075 K km $s^{-1}$. Circles at the top left corners represent the respective antenna beam size.

the CS map, the full resolution (6″) was used. However, the CCS map was smoothed to a 9″ beam in order to maximize the signal-to-noise ratio in the map.

## 3. RESULTS

The $C^{18}O$ (1–0) emission is proportional to the column density of gas, except in the very densest cores, and it gives an overall picture of the mass distribution in TMC-1. Figure 1*a* shows our large-scale $C^{18}O$ integrated intensity map of TMC-1. While the $C^{18}O$ emission fills about two-thirds of the map, it is brightest along a ridge roughly 12′ wide extending along the diagonal axis about 35′ (limited by the boundaries of our map). This long diagonal filament (or cylinder) contains two smaller elliptical filaments, each roughly 5′ by 10′ in size. The $C^{18}O$ emission also shows several cores about 2′–4′ in diameter embedded in each of these elliptical features. The emission feature located near the middle of the upper border in this map is a portion of a different cloud TMC-1C (see Kitamura et al. 1993 for a full map of this region). Individual $C^{18}O$ (1–0) spectra have typical line widths (FWHM) about 0.8 km $s^{-1}$ and show single or sometimes blended double-peak line profiles. Figure 2 shows an example of a double-peaked $C^{18}O$ profile superimposed with a CCS spectrum at the same position. The two prominent peaks in the CCS line occur at about the same velocities as those of the $C^{18}O$ line, but the overall velocity dispersion in CCS is considerably narrower than that for $C^{18}O$.

Core D occupies a small region in the $C^{18}O$ map, as indicated by a rectangle in Figure 1*a*. Our CCS 22 GHz integrated intensity map of core D (Fig. 1*b*) shows smaller structures than are evident in the $C^{18}O$ map, which is consistent with the higher spatial resolution and the higher critical density for excitation of the CCS 22 GHz line. [The critical density for $C^{18}O$ (1–0) is about 1500 $cm^{-3}$, while that for the CCS 22 GHz transition is ≈few × $10^4$ $cm^{-3}$.] However, the location of the peaks and the sizes of the structures seen in this integrated intensity map of CCS do not necessarily trace the fragments in core D because of the presence of several velocity components in most of the spectra. Instead, as discussed below we need to use the velocity information as revealed in individual spectra, position-velocity, and spatial-spatial maps at different velocities to characterize the substructure of core D.

The CCS 22 GHz spectra at all positions (observed with Nyquist sampling) are shown in Figure 3. It can be seen that these lines have very complex shapes which change significantly even among adjacent positions at the 24″ sampling of the map. The signal-to-noise ratio of these spectra is very high so that the changes in line shape among adjacent Nyquist sampled positions are measures of changes in density, column

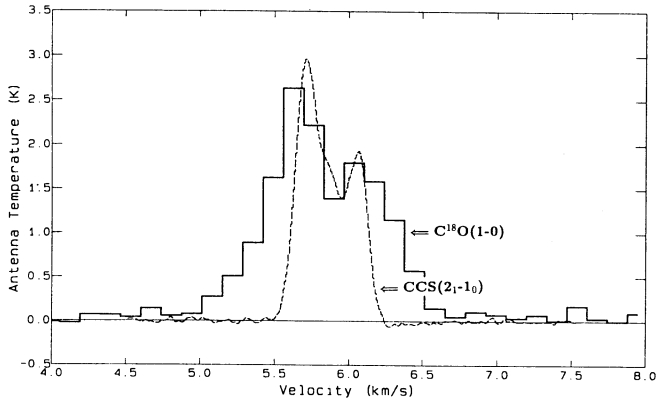


FIG. 2.—$C^{18}O$ and CCS spectra at the central position in TMC-1 core D (Fig. 1*a*). The $C^{18}O$ and CCS velocity channel widths are 0.14 and 0.008 km $s^{-1}$, respectively. The CCS spectrum was smoothed spatially to a lower resolution of 100″, corresponding to the angular resolution of the Bell Laboratories 7 m antenna.

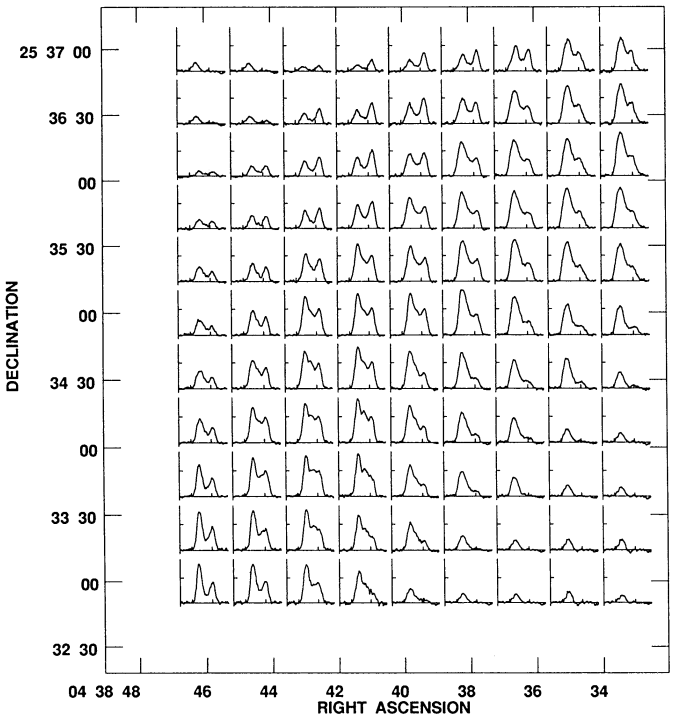


FIG. 3.—Plotted are all the CCS spectra at 22 GHz in core D taken with the 70 m antenna. The spectra were observed every 24″ in both north-south and east-west directions; the antenna beamwidth is 45″. The channel width is 0.008 km s$^{-1}$, and the spectra are smoothed to a velocity resolution of 0.025 km s$^{-1}$.

density, and chemical abundance, and hence structure, on a scale comparable to, or less than, the beam size of 45″. The explanation for such changes which we will advocate below is that, in addition to the emission from the extended structure of core D, several small clumps with narrow line widths $\lesssim$0.15 km s$^{-1}$ located along each line of sight contribute significantly. These clumps are likely to be embedded in larger, more diffuse gas as traced by $C^{18}O$. To establish this model for the CCS line shapes, we have to show that self-absorption is unimportant, that is, that the dips in the spectra are not absorption features, and that the opacity is not large. Furthermore, we need to determine a characteristic line width of a single component in the blended line.

To check for self-absorption or shadowing, we observed the map center position in CCS and $CC^{34}S$ ($J_N = 3_2$–$2_1$). These are plotted in Figure 4 along with CCS ($J_N = 2_1$–$1_0$) and the AT&T Bell Laboratories CCS ($J_N = 8_7$–$7_6$) spectrum. The CCS and $CC^{34}S$ ($J_N = 3_2$–$2_1$), which have the same spatial and spectral resolution, have similar line shapes. However, the three individual velocity features are more distinct in the more optically thin $CC^{34}S$. There is no evidence in these line shapes for self-absorption: all the features seen in CCS are seen in $CC^{34}S$. Thus, the dips in the CCS lines are not the result of foreground absorption. Furthermore, the CCS/$CC^{34}S$ line intensity ratio is $\sim$12–15 across the line profile, whereas the terrestrial (and probably interstellar) value of the sulfur isotopic ratio $^{32}S/^{34}S$ is 23. Thus, the 33 GHz line cannot be very optically thick and, if the excitation conditions are similar, the isotope ratio implies $\tau$(CCS $J_N = 3_2$–$2_1$) < 1.5 (at the line peak). We estimate the corresponding opacity at 22 GHz from an LVG excitation calculation (see § 4) to be $\tau$(CCS $J_N = 2_1$–$1_0$) < 0.7 (at the line peak). The $HC_3N$ profiles of Tölle et al.

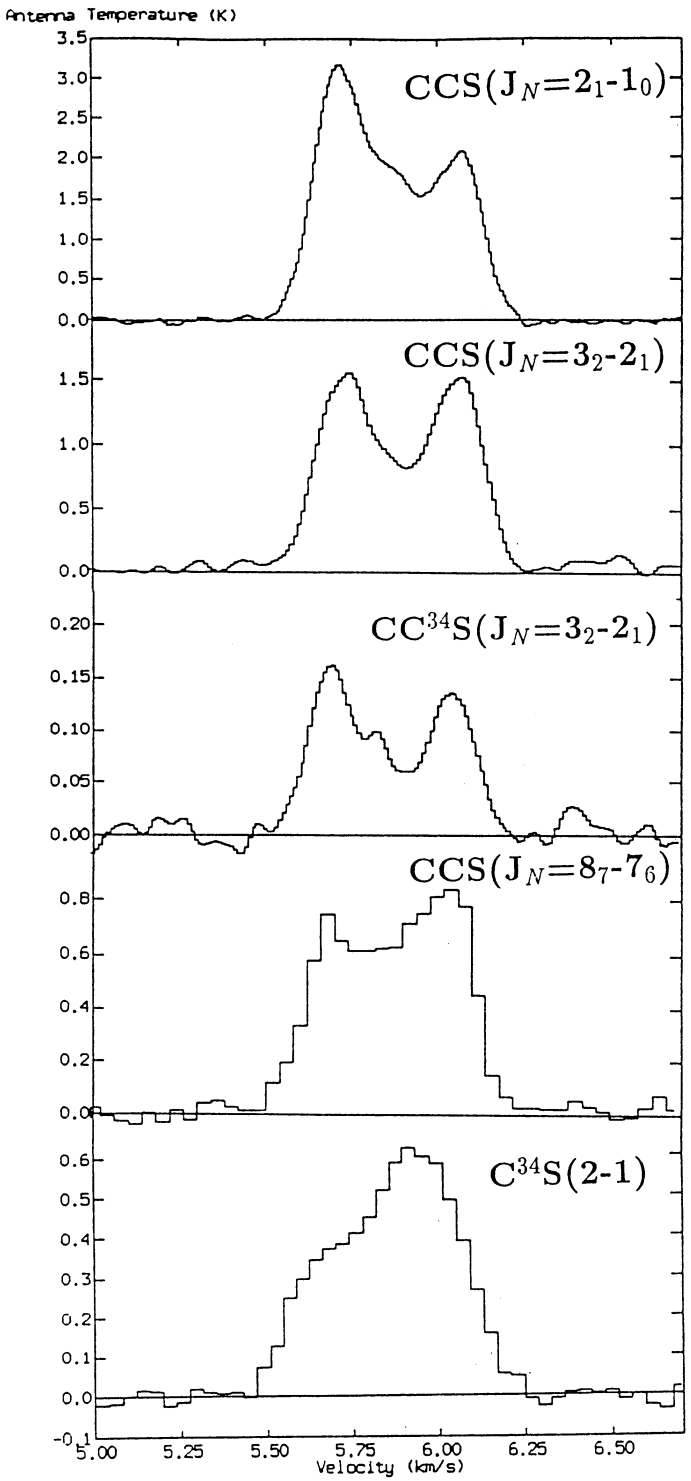


FIG. 4.—High spectral resolution lines in TMC-1 core D at the position R.A.(1950) = 04$^h$38$^m$42$^s$.0, decl.(1950) = 25°34′50″. The 22 and 33 GHz profiles are sampled every 0.008 and 0.011 km s$^{-1}$, respectively, and are smoothed to 0.025 and 0.04 km s$^{-1}$. The CCS 93 and $C^{34}S$ 96 GHz profiles have spectral resolutions of 0.04 km s$^{-1}$ and were taken with the 7 m antenna with $\sim$120″ beam.

(resolution of 0.030 km s$^{-1}$) are similar to our 22 GHz CCS profile, corroborating that the optical depth effects on the 22 GHz line shape are small.

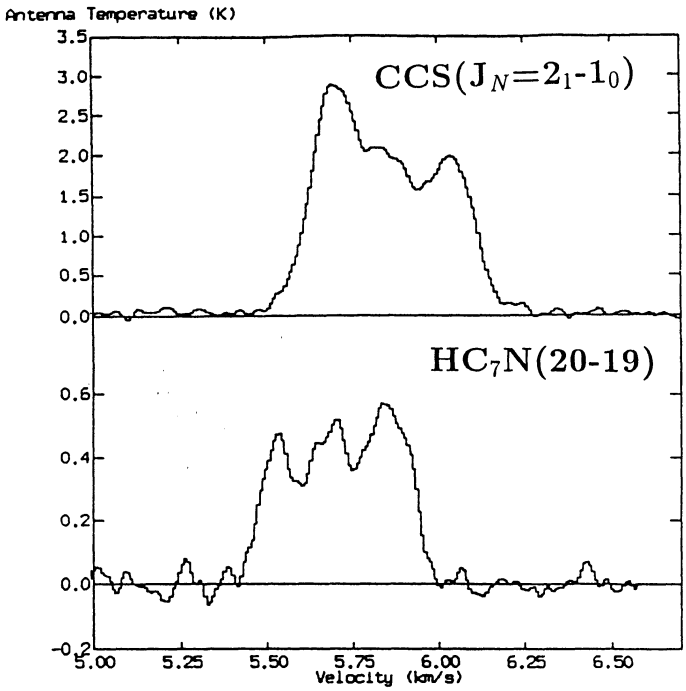


FIG. 5.—High spectral resolution lines of CCS and $HC_7N$ in TMC-1 core D at the position R.A.(1950) = $04^h38^m44^s3$, decl.(1950) = 25°34′14″. The 22 GHz profiles are sampled every 0.008 km $s^{-1}$ and are smoothed to 0.025 km $s^{-1}$. The $HC_7N$ lines show three distinct components, and the central and high velocity features are probably composed of two blended velocity components. The $HC_7N$ frequencies were calculated from the molecular constants and the shift in velocity with respect to CCS is caused by the uncertainties in the frequencies. We did not correct the $HC_7N$ frequencies to line up with those of CCS.

Figure 5 shows our 22 GHz $HC_7N$ and 22 GHz CCS spectra at a position 48″ from the center. This position was chosen for $HC_7N$ spectrum because the three velocity components are seen very prominently here. The $HC_7N$ line is shifted in velocity with respect to the CCS line, which we believe is caused by the uncertainty in the calculated $HC_7N$ frequency (see § 2). Because $HC_7N$ is 1.8 times more massive than CCS, it has an even narrower intrinsic thermal line width (by a factor of 25%) and the various overlapping velocity components separate better than in CCS. The overall width of the $HC_7N$ line at the base (hyperfine splitting is negligible for this transition) is about 15% narrower than for CCS, which is a consequence of the narrowing of the individual outermost components that make up the line profile. Three component Gaussian fits to the $HC_7N$ line profile yield very narrow line widths ranging from 0.11 to 0.15 km $s^{-1}$ (see Table 2). We can see some indication for the presence of additional components, especially in the high-velocity feature of the $HC_7N$ spectrum which has a non-Gaussian shape.

## 4. ANALYSIS

The line profiles in Figures 3–5 show at least three major components, each with spatial structure. The CCS spectra in Figure 3 show that the emission in these three components is widely distributed along the southeast-northwest filament, but their intensities vary significantly from one position to the other, even at the Nyquist sampling of 24″, over almost the entire mapped region. These changes are real, rather than a result of noise or baseline effects, since the signal-to-noise ratios of all the spectra are very high. As noted above, such changes are indicative of structural variations on a scale of the beamwidth (45″) or smaller. The variations in the line spectra from position to position indicate that several small features are embedded in a larger scale structure of each of these velocity components.

We have chosen to identify the clumps by the peaks in the CCS 22 GHz emission in the velocity channel maps. The term "clump" generally implies a distinct spatially localized density feature. The emission peaks are probably column density peaks and could be chemical abundance peaks. Because we find that the emission peaks are spatially localized in right ascension and declination, it is likely that they are also localized along the line of sight. Therefore, we believe that they are not only column density enhancements but also local density enhancements. However, we cannot exclude the fact that emission peaks are chemically enhanced, since the CCS abundance is believed to vary significantly with density and time (Suzuki et al. 1992). For positions where we have higher excitation and/or higher resolution information (see below) from the VLA and OVRO-MMA, the local peaks appear to be clumps. Thus, it seems reasonable to assume that all the emission peaks correspond to clumps with enhanced density.

When we fit the $CC^{34}S$ ($J_N = 3_2$–$2_1$) line with a combination of three Gaussians, we find (Table 2) that the peak line velocities are 5.68, 5.83, and 6.03 km $s^{-1}$ and that each feature has a corresponding line width of 0.15, 0.12, and 0.17 km $s^{-1}$. Although the line width for the central component in the $CC^{34}S$ lines is as narrow as 0.12 km $s^{-1}$, typical CCS line width components are 0.2 km $s^{-1}$. The parameters for all the lines shown in Figures 4 and 5 are given in Table 2. Though the line parameters are given to two decimal place accuracy, in many cases the errors to the velocities are even smaller, only a few meters per second. These three velocity features have different excitation temperatures, as is evident from the intensity ratios among the 22, 33, and 93 GHz CCS lines, and the CCS isotope ratio at 33 GHz. Thus, the density and CCS fractional abundances of the three main components vary. The relative peak intensities of $HC_7N$ to CCS also change among the three main velocity components, which could be the result of $HC_7N$ and/or CCS abundance variations.

### 4.1. *Large-Scale Spatial Structure*

Disentangling the components in a map from the spectral and spatial information is a long-standing and difficult problem. Various techniques have been applied in the literature including using the half-power contours, structure tree analysis (Houlahan & Scalo 1992), connected local minima as used in Clumpfind (Williams et al. 1994), Gaussian decompositions (Stutzki & Gusten 1990), and multiscale transforms (Langer, Wilson, & Anderson 1993). There is no uniform agreement as to which (if any) is the best approach to this problem. Furthermore, they generally work best on maps with a larger database than our CCS one. Therefore, we have decided to take a traditional approach to estimate the number of clumps by visual inspection of the peaks and contour levels in both position-velocity (P-V) and individual spatial-spatial maps for different velocity channels. The P-V map along the major (southeast to northwest) axis (Fig. 6) has about 8–10 spatial velocity features (clumps) within a 6′ × 1′ slice, as determined

TABLE 2

RESULTS OF GAUSSIAN FITS TO LINE PROFILES AT SELECTED POSITIONS

| Transition | GHz | $T_A^*$ (K) | $V_{lsr}$[a] (km s$^{-1}$) | $\Delta V$[a] (km s$^{-1}$) | Position Offset[b] (″,″) |
|---|---|---|---|---|---|
| | | Component 1 | | | |
| CCS ..... | 22 | 2.45 ± 0.03 | 5.70 ± 0.01 | 0.16 ± 0.01 | (0, 0) |
| | 33 | 1.44 ± 0.12 | 5.72 ± 0.01 | 0.16 ± 0.02 | (0, 0) |
| | 93 | 0.67 ± 0.03 | 5.70 ± 0.01 | 0.24 ± 0.02 | (0, 0) |
| $CC^{34}S$..... | 33 | 0.161 ± 0.002 | 5.68 ± 0.01 | 0.15 ± 0.01 | (0, 0) |
| $C^{34}S$..... | 96 | 0.289 ± 0.116 | 5.64 ± 0.02 | 0.20 ± 0.03 | (0, 0) |
| $C^{18}O$..... | 109 | 2.47 ± 0.07 | 5.64 ± 0.02 | 0.45 ± 0.04 | (0, 0) |
| CCS ..... | 22 | 2.82 ± 0.05 | 5.71 ± 0.01 | 0.17 ± 0.01 | (+31, −36) |
| $HC_7N$..... | 22 | 0.435 ± 0.016 | 5.52 ± 0.01 | 0.11 ± 0.01 | (+31, −36) |
| | | Component 2 | | | |
| CCS ..... | 22 | 1.75 ± 0.03 | 5.87 ± 0.01 | 0.27 ± 0.04 | (0, 0) |
| | 33 | 0.744 ± 0.05 | 5.86 ± 0.01 | 0.18 ± 0.12 | (0, 0) |
| | 93 | 0.76 ± 0.07 | 5.96 ± 0.02 | 0.20 ± 0.06 | (0, 0) |
| $CC^{34}S$..... | 33 | 0.078 ± 0.003 | 5.83 ± 0.01 | 0.12 ± 0.01 | (0, 0) |
| $C^{34}S$..... | 96 | 0.548 ± 0.492 | 5.89 ± 0.19 | 0.29 ± 0.27 | (0, 0) |
| $C^{18}O$..... | 109 | ... | ... | ... | (0, 0) |
| CCS ..... | 22 | 1.80 ± 0.07 | 5.87 ± 0.01 | 0.16 ± 0.01 | (+31, −36) |
| $HC_7N$..... | 22 | 0.491 ± 0.011 | 5.68 ± 0.01 | 0.15 ± 0.01 | (+31, −36) |
| | | Component 3 | | | |
| CCS ..... | 22 | 1.63 ± 0.14 | 6.08 ± 0.01 | 0.15 ± 0.01 | (0, 0) |
| | 33 | 1.56 ± 0.05 | 6.06 ± 0.01 | 0.18 ± 0.02 | (0, 0) |
| | 93 | 0.52 ± 0.26 | 6.08 ± 0.01 | 0.10 ± 0.03 | (0, 0) |
| $CC^{34}S$..... | 33 | 0.140 ± 0.002 | 6.03 ± 0.01 | 0.17 ± 0.01 | (0, 0) |
| $C^{34}S$..... | 96 | 0.217 ± 0.106 | 6.04 ± 0.09 | 0.20 ± 0.18 | (0, 0) |
| $C^{18}O$..... | 109 | 1.58 ± 0.10 | 6.16 ± 0.02 | 0.42 ± 0.05 | (0, 0) |
| CCS ..... | 22 | 1.91 ± 0.06 | 6.04 ± 0.01 | 0.17 ± 0.01 | (+31, −36) |
| $HC_7N$..... | 22 | 0.570 ± 0.013 | 5.86 ± 0.01 | 0.14 ± 0.01 | (+31, −36) |

[a] The values are rounded off to two decimal places; the errors in most cases are only a few m s$^{-1}$.

[b] (0,0) is at R.A.(1950) = 04$^h$38$^m$42$^s$.0, decl.(1950) = 25°34′50″.

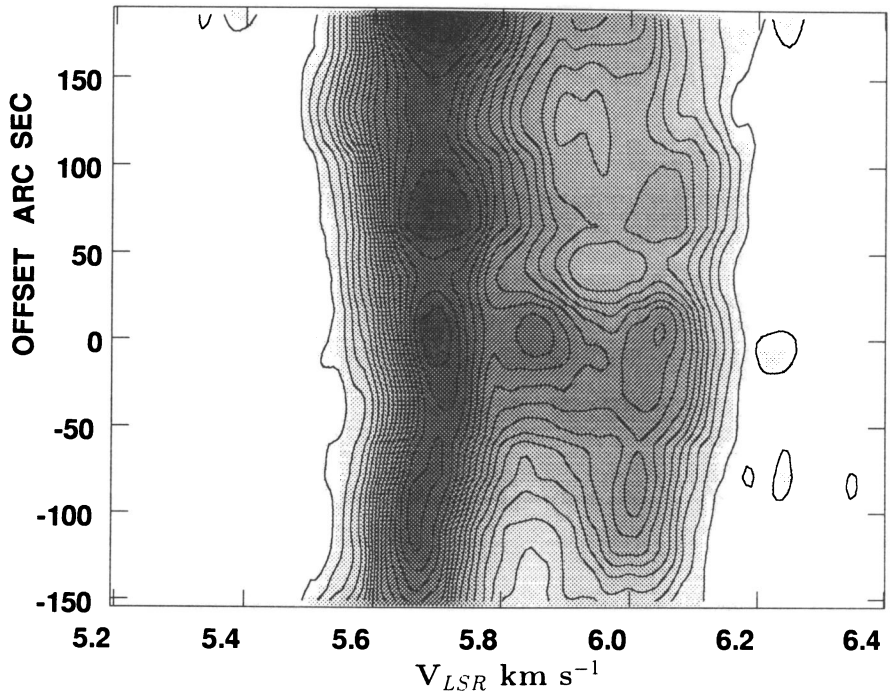


FIG. 6.—CCS position-velocity map of core D along the southeast to northwest direction approximately passing through the three peaks in Fig. 1*b*. Velocity and angular resolutions are 0.025 km s$^{-1}$ and 45″ respectively, but sampled at 0.008 km s$^{-1}$ and 24″. The first contour and interval are 0.15 K and the rms = 0.04 K. There are eight separate features along this cut with sizes about 45″–90″.

from isolating individual peaks. The angular extent of the velocity components in the P-V map ranges from 45″ to 90″, as can be seen from the size of closed contours.

Figure 7 shows the individual CCS channel spatial-spatial maps of the inner region at velocity intervals of 0.05 km $s^{-1}$ covering the spectrum from 5.49 to 6.24 km $s^{-1}$. The lowest contour and the contour intervals in Figure 7 are more than 6 times the rms noise, and therefore the local peaks (and even the map boundaries) are statistically significant. A high degree of clumpiness in the core is evident in these maps. Visual inspection shows that there are at least eight distinct clumps which are marked *a–h*. The parameters for these clumps are listed in Table 3. The $V_{lsr}$ and line widths of the clumps were obtained by fitting a multiple Gaussian to the line profile for each clump position. The CCS clump line widths range from 0.15 to 0.20 km $s^{-1}$. A rough estimate of size, based on closed contours around the peaks, yields a range of clump sizes 45″–90″. The differences seen in the adjacent channel maps, which are only 0.05 km $s^{-1}$ apart, show that there is significant blending of velocity components in the spectra. Therefore, it is likely that more features contribute to the emission in these maps, but it would require higher spatial resolution, such as that possible with interferometers, to separate these.

### 4.2. *Small-Scale Structure: Interferometric Observations*

Three of the clumps which we have identified in Figure 7 appear to be less than 60″ (0.04 pc) in size and are barely, if at all, resolved spatially in the 70 m beam (even though they are isolated in velocity space). To characterize these structures and to search for any smaller scale substructure, we were able to make interferometric observations with the VLA and OVRO-MMA over a limited area of core D. As a result of the narrow line width of the components, we had to use extremely narrow channel widths for the VLA and OVRO observations, 3 and 16 kHz, respectively.

In Figures 8 and 9 are shown the CCS and CS spectra obtained with the interferometers at the VLA and OVRO-MMA. For comparison we also show in both figures the 70 m single-dish CCS spectra at 22 GHz. The VLA spectra were obtained using the channel maps made with a coarser spatial resolution (15″ × 15″). The OVRO spectra for CCS and CS correspond to the visibility in shortest baseline averaged over a

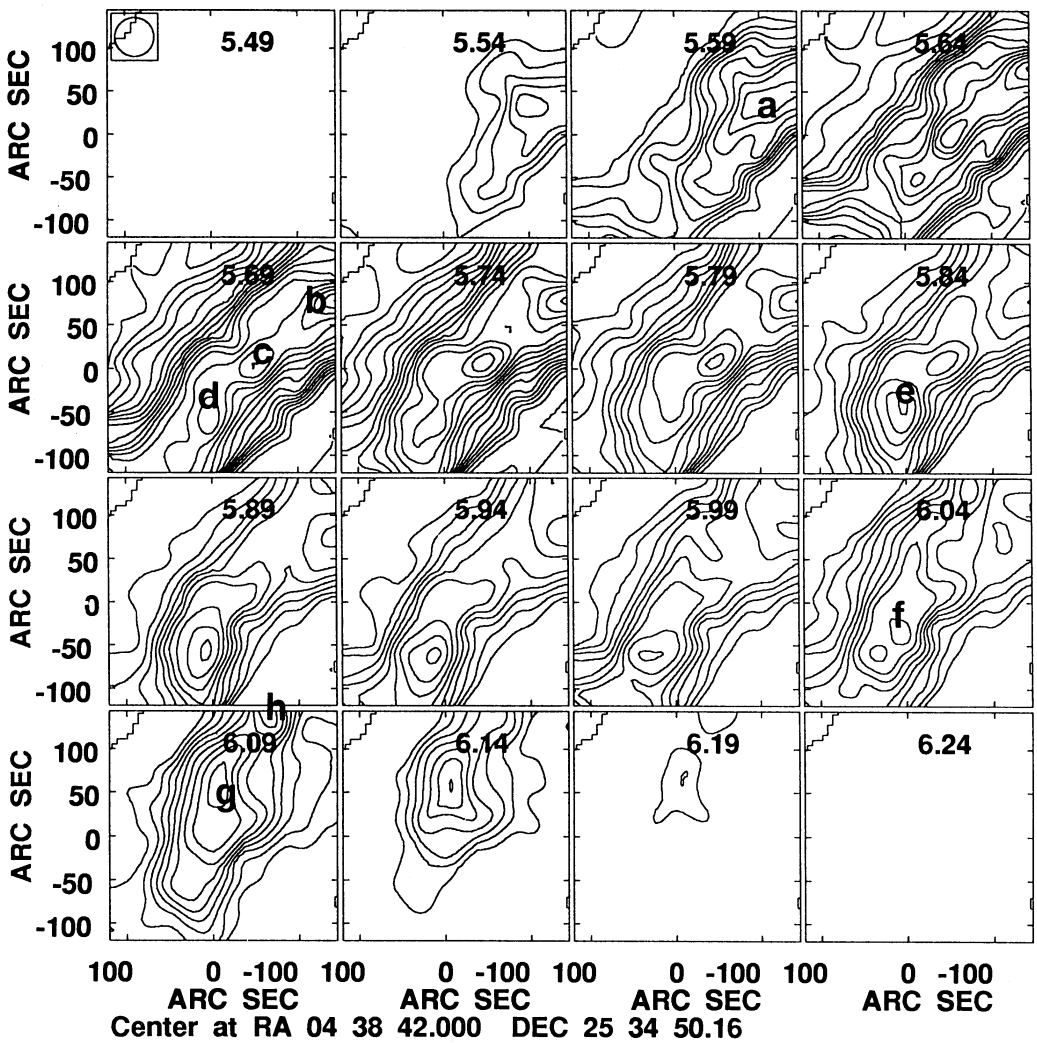


FIG. 7.—DSN 70 m CCS intensity spatial-spatial maps of TMC-1 core D; one map is shown for every 0.05 km $s^{-1}$ velocity interval. The contours are $T_A$ averaged over 0.05 km $s^{-1}$, and the lowest contour and contour interval are 0.2 K. Each map is centered at R.A.(1950) = $04^h38^m42^s.0$, decl.(1950) = 25°34′50″. The eight clumps we identify in the CCS data cube are labeled *a–h*. The circle at the top left corner represents the beam size.

TABLE 3

PARAMETERS FOR CLUMPS IDENTIFIED IN SINGLE-DISH SPATIAL-SPATIAL MAPS OF CCS

| Clump | $\Delta\alpha$ | $\Delta\beta$ | $T_A^*$ (K) | $V_{lsr}$ (km s$^{-1}$) | $\Delta V$ (km s$^{-1}$) | Size[a] |
|---|---|---|---|---|---|---|
| *a* ..... | −100″ | +30″ | 1.58 ± 0.61 | 5.63 ± 0.01 | 0.18 ± 0.02 | 100″ × 60″ |
| *b* ..... | −140 | +80 | 2.95 ± 0.65 | 5.69 ± 0.01 | 0.20 ± 0.02 | ... |
| *c* ..... | −50 | +00 | 1.72 ± 0.21 | 5.72 ± 0.01 | 0.17 ± 0.01 | 50 × 50 |
| *d* ..... | +00 | −60 | 3.06 ± 0.07 | 5.70 ± 0.01 | 0.17 ± 0.01 | 50 × 50 |
| *e* ..... | +05 | −40 | 2.15 ± 0.05 | 5.87 ± 0.01 | 0.16 ± 0.01 | 110 × 60 |
| *f* ..... | +10 | −30 | 1.82 ± 0.05 | 6.07 ± 0.01 | 0.15 ± 0.01 | <50 × 50 |
| *g* ..... | −10 | +50 | 1.75 ± 0.51 | 6.10 ± 0.01 | 0.15 ± 0.01 | 75 × 45 |
| *h* ..... | −60 | +140 | 1.63 ± 0.05 | 6.07 ± 0.01 | 0.15 ± 0.01 | ... |

[a] Based on the lowest closed contour around the peaks in Fig. 7.

range of spatial frequencies from 2500 to 6500 Å at their map centers. The 70 m and VLA CCS spectra are at the positions of clumps *g* and *f*, and the OVRO CCS spectrum is for clump *g*. The CS and CCS spectra shown in Figure 9 comes from a position 20″ east of the nominal center of core D. It may be noted that the 70 m single-dish spectra shown here contain spatial frequencies up to about 4000 Å and are weighted heavily by the shorter wavelengths less than 2000 Å. In contrast, the interferometer spectra contain only the spatial frequencies greater than 2500 Å and are weighted heavily by the higher frequencies.

Whereas the single-dish 22 GHz spectrum has the same intensity at the 5.7 and 6.1 km s$^{-1}$ components, in the VLA and OVRO-MMA spectra the 6.1 km s$^{-1}$ component is distinctly stronger. Because an interferometer acts as a spatial filter, its spectra contain emission from small-scale structures (<30″ for the VLA and OVRO-MMA). In the case of CCS emission, the small-scale structures are seen prominently only in the 6.1 km s$^{-1}$ velocity component (Fig. 8). The 5.7 km s$^{-1}$ component is relatively weak and does not have sufficient signal-to-noise ratio to generate a spatial map. The single-dish CCS 93 GHz spectrum in Figure 4 also shows that the 6.1 km s$^{-1}$ velocity component is more prominent. Since higher densities are required for the excitation of the CCS 93 GHz transition, it is likely to arise from denser and hence more compact clumps. Thus, these interferometric spectra show that the 6.1 km s$^{-1}$ velocity component contains regions of higher density and/or smaller sizes. For CS, in contrast to CCS, we only detect the 5.7 km s$^{-1}$ component (see Fig. 9*b*). All the interferometer spectra have very narrow line widths, <0.2 km s$^{-1}$. The high-resolution spatial-spatial maps of the CCS 6.1 km s$^{-1}$ and CS 5.7 km s$^{-1}$ components are shown in Figures 8 and 9. These maps were made by averaging the visibilities in three adjacent channels around the peaks in the spectra (line width of about 0.15 km s$^{-1}$). For comparison, we also show the single-dish CCS 22 GHz maps, which trace out the larger structures, at these two velocities.

The field of view of the primary beam of the VLA is 120″ and covers the central region of core D, as indicated by a box in Figure 8*d*. The clumps *f* and *g* (see Fig. 7, particularly the panels for 6.04 and 6.09 km s$^{-1}$) were detected in the VLA observations (Fig. 8) with intensities above the 5 $\sigma$ level. In the VLA map the small-scale structure of clump *g* is extended north-south and has an angular size FWHM of 20″ × 30″ with peak brightness of 3.0 ± 0.50 K. There is a suggestion of further structure in clump *g* in the VLA data, and it may be composed of two smaller clumps, as indicated by the two intensity peaks located along the north-south axis. Clump *f*, located in the lower part of the VLA map, is weaker and appears to be more diffuse spatially with one bright compact region with angular size about 10″ × 10″ (0.007 pc × 0.007 pc) and peak brightness of 2.5 ± 0.5 K. Although clumps *c* and *e* (as defined by the single-dish maps in Fig. 7 at $V_{lsr}$ = 5.69 and 5.84 km s$^{-1}$, respectively) are within the VLA primary beam, no significant emission was observed at their positions and velocities.

The largest scale structures that can be observed in a full synthesis D configuration VLA map at 22 GHz is ~60″. However, for the observations reported here we had only partial synthesis, and therefore structures larger than 40″ cannot be detected. The extremely narrow line width of the velocity components also severely limits the sensitivity of our observations, since we had to use narrow channel widths. The absence of any detectable emission from the parts of other clumps within the primary beam of the VLA suggests that they are likely to be resolved out and have sizes larger than 40″. The fraction of flux contained in the small-scale structures (size <30″) is less than 10%. For example, in Figure 8, the total flux density of the 6.1 km s$^{-1}$ component in the single-dish map over the VLA field of view is ~21 Jy, while the total flux density in the VLA map is only ~1.5 Jy.

The OVRO-MMA field of view is about 60″ at 93 GHz, much smaller than that of the VLA at 22 GHz. Given the weakness of the CCS signals and limited observing time, we restricted our OVRO-MMA observations to a field of view centered on clump *g*, the strongest feature in the VLA map. The 93 GHz CCS emission has been detected from clump *g* (Fig. 8), and this high spatial resolution map shows three dense embedded structures with even smaller sizes than the clump seen in the 22 GHz VLA map. (Our OVRO-MMA maps are not sensitive to structures larger than 30″ as a result of the missing short spacings.) Although the overall shape of the 93 GHz CCS emission is consistent with the VLA structure of clump *g*, the central peak is slightly displaced eastward (about 10″). The ratio of brightness temperatures of the 22 and 93 GHz CCS emission in these small-scale structures is in the range of 1.5–2.5. The 93 GHz transition traces densities 10–100 times larger than the 22 GHz transition, as determined from excitation models (see discussion below). Thus, the 93 GHz CCS emission indicates the presence of high-density small-scale internal structure in clump *g*. We would need higher sensitivity in the 93 GHz OVRO-MMA map (the signal-to-noise ratio at the peak is only 6) to investigate in more detail the density and velocity structure of clump *g*.

In Figure 9 we show the CS(2–1) OVRO-MMA spectrum and spatial-spatial map at $V_{lsr}$ = 5.7 km s$^{-1}$ (averaged over a line width of about 0.15 km s$^{-1}$; see the CS spectrum). The angular resolution of the map is 6″, and the rms is 0.08 Jy beam$^{-1}$. The peak brightness is 1.6 K, and the rms is 0.25 K. The CS clump is fully resolved and has an angular extent of

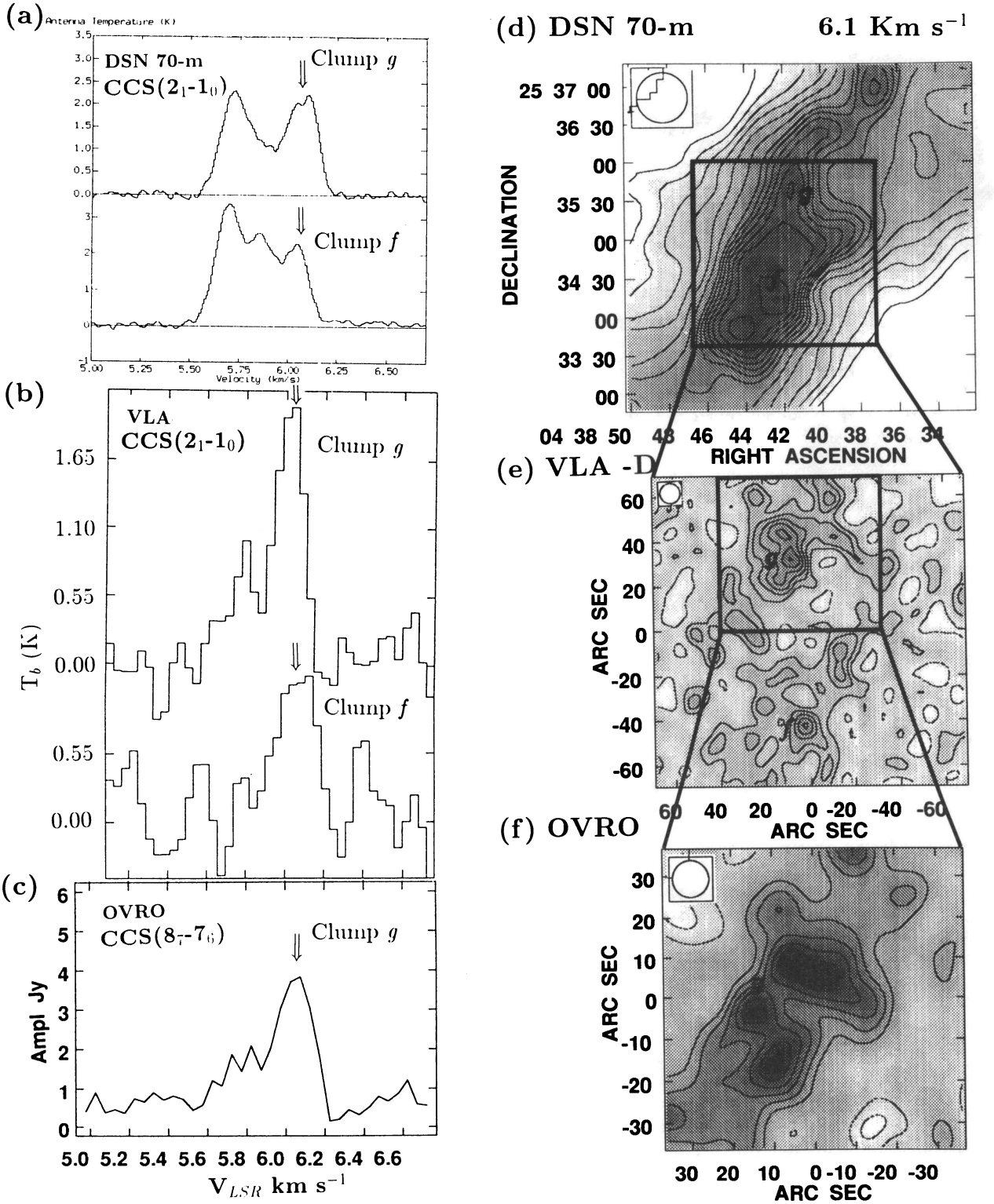


FIG. 8.—(*a*)–(*c*): CCS spectra of selected regions in TMC-1 core D mapped with the VLA and OVRA-MMA. (*a*) 70 m single-dish spectra at 22 GHz of clumps *g* and *f*, (*b*) VLA spectra at 22 GHz of clumps *g* and *f* obtained with a low-resolution 15″ beam; (*c*) OVRO-MMA spectrum at 93 GHz of clump *g* obtained by averaging the visibilities in the short spacings from 2500 to 6500 Å. The 6.1 km s$^{-1}$ velocity component is clearly detected in both the VLA and OVRO spectra. There is evidence for a second velocity component at 5.7 km s$^{-1}$ in both spectra. Arrows indicate the velocity (channel) of the maps shown in (*d*)–(*f*). (*d*)–(*f*): CCS spatial maps for the 6.1 km s$^{-1}$ velocity component in TMC-1 core D. Regions mapped with the VLA and OVRO are indicated by boxes. Spatial resolution in the 70 m, VLA, and OVRO maps is 45″, 9″, and 9″, respectively. The circle at the top left corner of the maps represents the beam size. (*d*) 70 m single-dish map at 22 GHz; (*e*) VLA map at 22 GHz centered at R.A.(1950) = 04$^h$38$^m$42$^s$.0, decl.(1950) = 25°34′50″; the first contour level and interval are 16 mJy beam$^{-1}$ (0.50 K in $T_b$); the rms noise in the map is 14 mJy beam$^{-1}$; (*f*) OVRO map at 93 GHz centered at R.A.(1950) = 04$^h$38$^m$42$^s$.3, decl.(1950) = 25°35′25″; the first contour level and interval are 120 mJy beam$^{-1}$ (0.20 K in $T_b$); the rms noise in the map is 90 mJy beam$^{-1}$. The VLA map shows a strong condensation at the position of clump *f* and several small-scale structures in clump *g*. The OVRO 93 GHz map traces several small-scale high-density condensations within clump *g*.

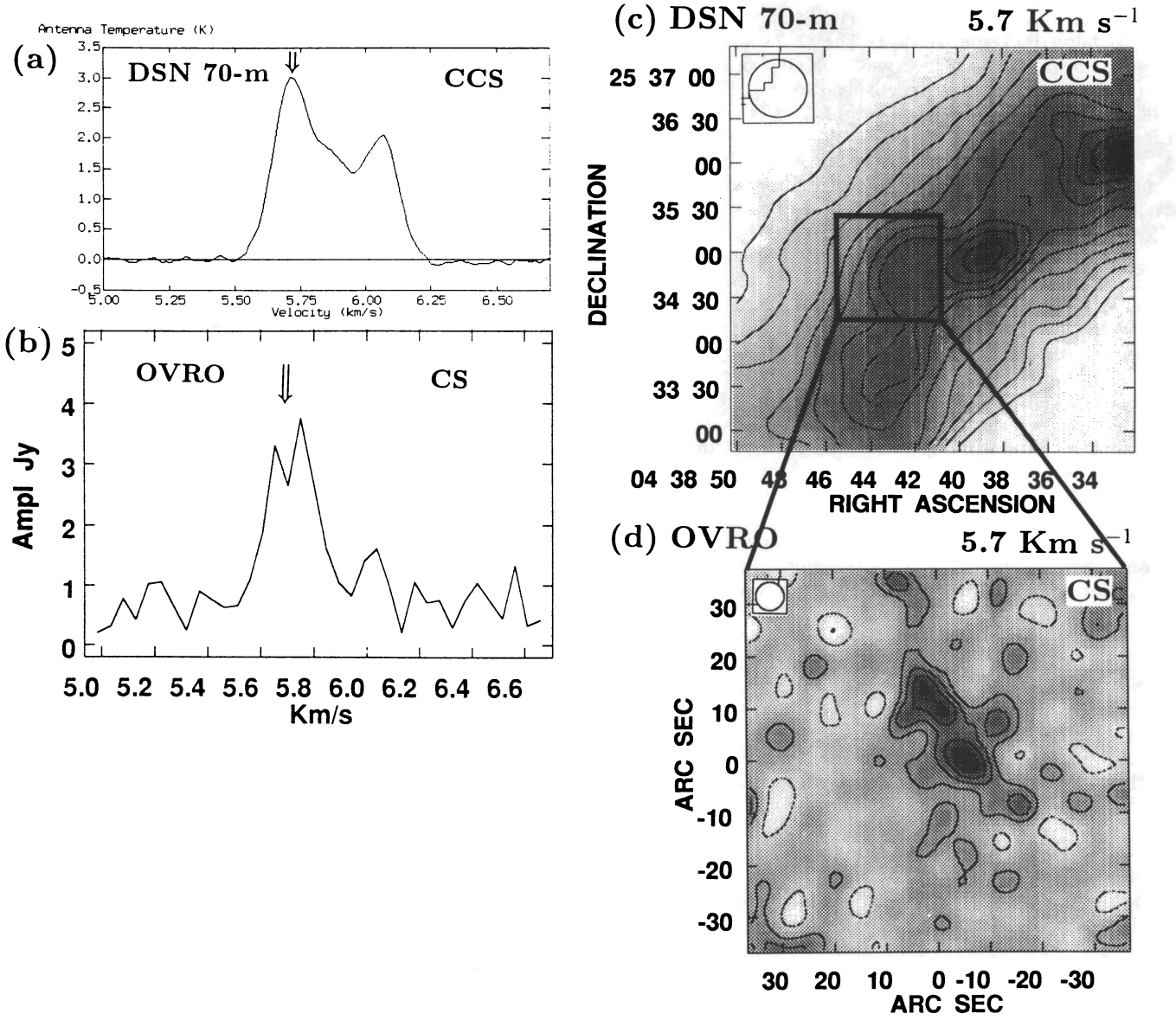


FIG. 9.—(*a*)–(*b*): CCS and CS spectra in TMC-1 core D at the center of the OVRO map region shown by a box in (*c*). (*a*) 70 m single-dish CCS spectrum at 22 GHz obtained with 45″ beam. (*b*) OVRO-MMA CS (2–1) spectrum at 98 GHz obtained by averaging the visibilities in the short spacings from 2500 to 6500 Å. The CS (2–1) spectrum shows prominent emission at 5.7 km s$^{-1}$. Arrows indicate the velocity (channel) of the maps shown in (*c*)–(*d*). (*c*)–(*d*): CCS and CS spatial maps for the 5.7 km s$^{-1}$ velocity component in TMC-1 core D. The region mapped with the OVRO-MMA is indicated by a box. Spatial resolutions in the 70 m and OVRO maps are 45″ and 6″, respectively. The circle at the top left corner of the maps represents the beam size. (*c*) 70 m single-dish map at 22 GHz. (*d*) OVRO map at 98 GHz centered at R.A.(1950) = 04$^h$38$^m$43$^s$.5, decl.(1950) = 25°34′50″; the lowest contour level and contour interval are 100 mJy beam$^{-1}$ (0.35 K in $T_b$); the rms noise in the map is 85 mJy beam$^{-1}$. The CS is concentrated in three or four small clumps located along a ridge running northeast-southwest. The CS feature is located at a position in the single-dish CCS map (*top*) that appears as a bulge. This position probably marks a separate 45″ clump that is blended in this map.

about 10″ × 24″ (0.007 × 0.016 pc) at the 3 $\sigma$ level. It is oriented northeast-southwest; that is, perpendicular to the orientation of the CCS emission at this velocity (Fig. 9*d*). The CS map shows evidence of substructure with two to three smaller clumps each ~10″ in diameter. The sensitivity in this map is not adequate for a detailed study of its velocity structure. We note also that no continuum emission at 98 GHz was detected at the 2 mJy (5 $\sigma$) level.

Interestingly, the CS clump does not show a spatial correspondence with any of the CCS clumps in the single-dish maps (see Fig. 7) or VLA maps (Fig. 8), although some enhanced CCS emission is seen at the velocity and position of the CS clump. The CS arises from a region that appears as a slight bulge, but not a distinct peak, in the CCS map. Most likely this region is a separate clump but one which cannot be clearly isolated from the surrounding emission. The lack of correspondence between the location of the CCS and CS clumps may indicate significant chemical differentiation over small distances (0.02–0.04 pc). Additional evidence for chemical differentiation can be seen by comparing the line shapes for CC$^{34}$S and C$^{34}$S (Fig. 4).

### 4.3. *Density Estimates*

We can determine the excitation conditions, density, and fractional abundance of the dense clumps in core D from the CCS and CC$^{34}$S lines. The energy levels, frequencies, and Ein-

stein $A$-values for CCS were calculated using the JPS Spectral Line Catalog (Pickett et al. 1991). The 22, 33, and 93 GHz lines originate from levels with energies (in K) of 1.6, 3.2, and 19.9 K above the ground state, respectively. (See Fig. 2 in Saito et al. 1987 for an energy level diagram for CCS.) The corresponding Einstein $A$-values are $4.3 \times 10^{-7}$, $1.6 \times 10^{-6}$, and $3.8 \times 10^{-5}$ $s^{-1}$. We adopt a large velocity gradient (LVG) model which should be a reasonable first approximation to calculate the excitation conditions. We use collision rates from A. Fuente (1994, private communication) and Wolkovitch et al. (1995), and, unless otherwise stated, a kinetic temperature of 10 K (Fuller & Myers 1993). The 22 and 93 GHz lines have critical densities $n(H_2)$ about $5 \times 10^4$ and $10^6$ $cm^{-3}$, respectively.

Presently we have multitransition information at the central position in the single-dish maps and can derive the excitation conditions only for the two clumps with size about 45″–60″ along this line of sight. We are currently undertaking a program to map all of core D at 45 and 93 GHz with 45″ angular resolution using the DSN and FCRAO antennas and will report on its density structure in a later paper (Wolkovitch et al. 1995). To derive the average density over 2′, we first convolved the lower frequency 22 GHz data to the 120″ resolution of the AT&T Bell Laboratories 93 GHz observations. We also used the 33 GHz data obtained with 70″ angular resolution to constrain the solutions of density, $n(H_2)$, and fractional abundance, $X$(CCS). The brightness temperatures of the source were calculated from the antenna temperatures at 22, 33, and 93 GHz using the corresponding beam efficiencies of 70%, 70%, and 95%. For the 5.7 km $s^{-1}$ component we find a density $\sim 2 \times 10^4$ $cm^{-3}$ and a CCS fractional abundance of $\sim 2 \times 10^{-9}$. For the 6.1 km $s^{-1}$ component the corresponding average density is $5 \times 10^4$ $cm^{-3}$ with a fractional abundance of $4 \times 10^{-10}$. We estimate from a parameter sensitivity study of the LVG solutions that these values are accurate to within a factor of a few. We will present our LVG models in more detail in a later paper on CCS excitation (Wolkovitch et al. 1995). These densities are consistent with those derived from CS by Snell et al. (1982) at the same resolution of 120″.

On a smaller scale of 45″, the 93 GHz brightness temperature is about 30% stronger than the Bell Laboratories spectra (this was determined by comparing the 7 m data to recent observations of the central position made with FCRAO's 14 m antenna; Wolkovitch et al. 1995). Thus, at the central position of core D we can estimate the density averaged over 45″ from the FCRAO results in conjunction with the 22 GHz spectrum taken with the same resolution. We find a density of $3 \times 10^4$ $cm^{-3}$ and a fractional abundance of $2 \times 10^{-9}$ at 5.7 km $s^{-1}$ and $8 \times 10^4$ $cm^{-3}$ and $10^{-9}$ for the 6.1 km $s^{-1}$ components.

For the smaller features seen in the VLA and OVRO-MMA maps ($\simeq$10″–30″), we can place bounds on the density using the brightness of the 22 and 93 GHz lines in conjunction with the LVG model. Inspection of the excitation solutions shows that the ratio of the 93 to 22 GHz brightness increases with density up to about $10^6$ $cm^{-3}$, where the lines become thermalized. First the density has to be greater than that estimated for the 45″ features ($> 8 \times 10^4$ $cm^{-3}$) as they are seen in both VLA and OVRO-MMA maps. Second, the density has to be $< 2 \times 10^6$ $cm^{-3}$, or else the features would be much brighter than observed in our OVRO-MMA CCS maps. Combining the interferometer line brightness with the single-dish measurements provides an estimate of the total line brightness. The small-scale structure in the VLA map ($T_b \sim 3$ K) is embedded in a background of about 1 K, as seen from the single-dish data. In the case of 22 GHz emission, all densities ($> 10^4$ $cm^{-3}$) along the line of sight contribute approximately equally to the total line brightness; but at 93 GHz, the highest densities dominate. The differences in the $u$-$v$ coverage of the VLA and OVRO-MMA maps make it difficult to estimate accurately the total line brightness at the two frequencies. Within the uncertainties in combining single-dish to interferometer maps, we can place limits on the maximum and minimum total brightness in the VLA map to be about 3.5 and 6 K. Combining the OVRO-MMA and single-dish observations yields a maximum brightness for 93 GHz of 2.5 K. The highest density is obtained by taking the minimum brightness for the 22 GHz line and the maximum brightness for the 93 GHz line. Thus, the density and CCS fractional abundance for the minimum and maximum brightness limits are $8 \times 10^4$ $cm^{-3}$ and $10^{-9}$ and $5 \times 10^5$ $cm^{-3}$ and $5 \times 10^{-11}$. The most likely values are $n(H_2) \sim 3 \times 10^5$ $cm^{-3}$ and $X(\mathrm{CCS}) \sim 2 \times 10^{-10}$. Densities greater than $10^6$ $cm^{-3}$ are almost certainly excluded, unless the kinetic temperature is about 6–7 K. (Our excitation analysis shows that the brightness in the VLA maps is consistent with kinetic temperatures $>6$ K.) We note also that there is some indication for decreasing fractional abundance of CCS with increasing densities. To derive both the kinetic temperature and density, we need more data on these small fragments in another transition, preferably at 45 GHz.

### 4.4. *Mass Estimates*

We have identified several features in our $C^{18}O$ map (Fig. 1*b*) from local peaks and closed contours. Some of these bear a similarity to the six features identified by Snell et al. (1982) from their CS (1–0) map of TMC-1. We can estimate the mass of these features using $C^{18}O$ as a column density tracer of molecular hydrogen, $N(H_2)$. Assuming that $C^{18}O$ is optically thin and thermalized,

$$N(H_2) = 9.9 \times 10^{20}[1 - \exp(-5.3/T_x)]^{-1} \times \int T_b(C^{18}O)dV \ \mathrm{cm}^{-2}$$

(Pound, Bania, & Wilson 1990), where we use the $C^{18}O$ fractional abundance determined by Frerking, Langer, & Wilson (1982) for the Taurus region. The mass is obtained by integrating the column density over the projected area, $A$, and multiplying by the molecular weight per particle (mainly to account for helium),

$$M(H_2) = \mu m(H_2) \int N(H_2)dA \ .$$

From the peak brightness temperature of $^{13}CO$ (not shown here) and our $C^{18}O$ spectra, we calculate that the excitation temperature lies in the range 6–9 K. Here we adopt $T_x = 7$ K, and the results differ by at most $\pm 20\%$ at the limits of the range for $T_x$. We have applied these formulae to all the features identified in the $C^{18}O$ map. In Table 4 we summarize the size and mass of the characteristic structures in TMC-1. The size and mass of the entire TMC-1 ridge (or cylinder) are 0.4 pc $\times$ 1.2 pc and 30 $M_\odot$. The two smaller elliptical filaments along this ridge are similar in size and have nearly identical masses, $\sim 10$ $M_\odot$. The seven or eight $C^{18}O$ cores along TMC-1 have masses in the range 0.6–2.5 $M_\odot$. The mass within the box around core D (Fig. 1*a*) is 2.2 $M_\odot$. The mass we derive

TABLE 4

PARAMETERS OF THE CHARACTERISTIC SUBSTRUCTURE IN TMC-1

| Structure | Tracer | Size (pc) | $n(H_2)$ ($10^4$ cm$^{-3}$) | Mass ($M_\odot$) | Virial Mass[a] ($M_\odot$) | Comments |
|---|---|---|---|---|---|---|
| TMC-1 | $C^{18}O$ | 1.2 × 0.4 | ... | 30 | 52 | bound |
| SE filament | $C^{18}O$ | 0.6 × 0.25 | ... | 10 | 29 | bound |
| Cores | $C^{18}O$ | 0.1–0.2 | ... | 0.5–3.2 | 5–15 | bound |
| Core D | CCS | 0.18 × 0.12 | 2 | 2.0 | 3.6 | bound |
| Clumps | CCS | 0.04 | 5 | 0.1 | 0.96 | unbound? |
| Small fragments | CCS | 0.01 | 30 | 0.01 | 0.24 | unbound-transient |

[a] Using $\Delta V = 0.85$ and 0.48 km s$^{-1}$, respectively for $C^{18}O$ and CCS tracers.

from $C^{18}O$ over the entire TMC-1 ridge agrees very well with the value of 20–35 $M_\odot$ derived from CS (Snell et al. 1982; Schloerb & Snell 1984).

We can use the CCS maps to estimate the mass of the smaller features embedded in core D. As noted above, we do not have sufficient information to determine the density and mass of every feature within the CCS single-dish and interferometer maps. However, the characteristics of the strongest clumps are similar enough to allow us to characterize the core properties from the few features where we have multitransition information. We estimate the mass of these various clumps seen in CCS using their size and mean density.

We calculate the total mass of core D using the average density, $2 \times 10^4$, derived from the CCS spectra smoothed to 120″, the resolution of the Bell Laboratories antenna at 93 GHz. This yields a total mass of 2.1 $M_\odot$, in good agreement with the mass calculated from $C^{18}O$ column density. For the clumps just resolved in the 70 m maps with angular size ~60″ (0.04 pc), the density is $\sim 5 \times 10^4$ cm$^{-3}$ and clump mass is ~0.1 $M_\odot$. For the small clumps within clump *g* resolved in the VLA and OVRO-MMA maps, ~20″, the density is $\sim 3 \times 10^5$ cm$^{-3}$, and the mass is ~0.02 $M_\odot$. For the smallest fragments just barely resolved in the VLA and OVRO-MMA maps with size ~10″ (0.007 pc) and density $\leq 10^6$ cm$^{-3}$, their mass is likely to be very small (<0.01 $M_\odot$).

## 5. DISCUSSION

Our large-scale $C^{18}O$ map shows some indication of hierarchical fragmentation in TMC-1 with dense cores of size 0.1–0.2 pc embedded in larger elliptical features (0.25 pc × 0.5 pc) which are themselves part of a long filamentary, or cylindrical, structure. From the CCS single-dish and interferometric maps of one of these cores, core D, we find evidence that TMC-1 probably contains many more small clumps than previously suspected. There are at least eight clumps seen in the single-dish maps of CCS with sizes about 60″ (0.04 pc) at $V_{lsr}$ between 5.6 and 6.1 km s$^{-1}$. At least two of these, *f* and *g*, contain small-scale structure as seen in the VLA and OVRO-MMA CCS maps at 6.1 km s$^{-1}$ and in the OVRO-MMA CS map at 5.7 km s$^{-1}$. There is also a hint of structure in our VLA CCS map at 5.7 km s$^{-1}$ (see spectrum in Fig. 8*b*), but the signal-to-noise ratio is not good enough for this velocity component to produce a reliable, high-resolution map. At least one of these clumps is composed of, or contains, three to six smaller scale components with sizes about 0.01 pc as seen in both our VLA and OVRO-MMA maps. These small-scale structures in the interferometer maps may represent high-density condensations or fragments within the clumps. Our best estimate of the density of these small fragments in $n(H_2)$ about $3 \times 10^5$ cm$^{-3}$ and CCS fractional abundance about $2 \times 10^{-10}$.

The CCS line widths are very narrow (both in the single-dish and interferometric spectra) and are composed of a thermal and nonthermal component. The velocity dispersion resulting from turbulent motions, $\sigma_{turb}$, within the clumps can be obtained from the CCS line widths by

$$\sigma_{turb} = \sqrt{\sigma_{tot}^2 - \sigma_{therm}^2} ,$$

where the total dispersion, $\sigma_{tot}$, is related to the line $\Delta V = 2.35\ \sigma_{tot}$.

The velocity dispersion resulting from thermal motions is

$$\sigma_{therm} = 0.0912 \sqrt{\frac{T}{m_{AMU}}}\ (\text{km s}^{-1}) ,$$

where $m_{AMU}$ is the molecular mass given in amu. For CCS at 10 K, the thermal velocity dispersion is 0.0386 km s$^{-1}$. A value of $\Delta V < 0.15$ km s$^{-1}$ implies a turbulent velocity dispersion less than 0.05 km s$^{-1}$, which is smaller than the sound speed (0.19 km s$^{-1}$) in a gas with mean molecular weight of 2.3 amu. Thus, the thermal pressure caused by molecular hydrogen at 10 K (corresponding to $\Delta V = 0.48$ km s$^{-1}$) is much greater than the turbulent pressure even in the larger fragments. From a comparison of the $HC_7N$ and CCS line widths in Table 2, we estimate $\sigma_{turb}$ to be <0.06 km s$^{-1}$. Thus, thermal pressure (caused by molecular hydrogen) is dominant in the core and the clumps, and turbulence is not a significant factor in their support.

Table 4 lists masses derived from $C^{18}O$ column densities and densities estimated from CCS line intensities for different (larger to smaller) scale size structures observed in TMC-1. We can draw some conclusions about the stability of these structures by comparing these masses with the corresponding virial mass $M_{vir}$. The virial masses listed in Table 4 were estimated using the relation $M_{vir} = 210\ R\ (\Delta V)^2$, taken from MacLaren, Richardson, & Wolfendale (1988) for constant density distribution. For the large-scale structures traced by $C^{18}O$, we used $\Delta V = 0.85$ km s$^{-1}$, the mean width of the $C^{18}O$ profile (Fig. 2). In the case of the small-scale structures traced by CCS, as described above, turbulence is negligible and we have to consider only the thermal pressure of $H_2$. Therefore, for $\Delta V$ we used the thermal line width for $H_2$ molecules at 10 K. The virial masses estimated assuming constant density are not very different (less by 15%) for a $1/r$ density distribution. If a structure has mass $M > \frac{1}{2} M_{vir}$ it is bound, and if $M \geq M_{vir}$ it will be unstable to collapse. The structures with $M < \frac{1}{2} M_{vir}$ are unbound. However, when applying the above criteria, one must be aware of the rather high uncertainties in the mass estimates (within a factor ~2 from $C^{18}O$ and, factors of about 2 and 10 from CCS observations for the 60″ and 10″ structures,

respectively). The properties of the different features indicated in Table 4 represent the most likely structure suggested by our observations.

Overall, core D appears to be bound but is not likely to be unstable against collapse. However, the smaller structures within this core are unbound. The clumps which are barely resolved in the single-dish maps ($\sim$45″–60″) appear to be unbound, or at most a few may be marginally bound. Those clumps resolved in the interferometers with sizes $<$20″ have a virial mass much greater than their actual mass. Hence, it appears that the features traced by CCS from 10″ to 30″ are most likely unbound and subject to expansion unless they are pressure confined. The presence of such unbound clumps within a cloud core suggests that fragmentation mechanisms other than a pure Jeans gravitational instability may be important in cold dense cores. Since the mass estimated from the density for the smaller fragments is an order of magnitude less than the virial mass, the clumps cannot be bound unless they have much higher densities, $\sim 10^7$ cm$^{-3}$. Although such a high density is not evident in the data presented here, it cannot be ruled out *if* the kinetic temperature is much lower than 10 K, about 6 or 7 K.

It has been suggested, on the basis of the $NH_3$ abundance, that the southeastern part of the TMC-1 filament (which includes core D) contains the youngest cores (Tölle et al. 1981; Olano et al. 1988; Hirahara et al. 1992). Thus, the clumpiness observed with CCS may describe the physical and chemical condition of the gas at very early stages of clump formation and evolution. The single-dish CCS maps show that the fragments are distributed along the filament and that they have a very narrow width perpendicular to the filament. Our high-resolution OVRO-MMA and VLA maps resolve the structure perpendicular to the filament at some places into small-scale structures. Carbon chain molecules (CCS and cyanopolyynes) may be produced most efficiently in small fragments with enhanced densities. The density enhancements seen along the southeast-northwest filamentary-like structure may arise from fragments formed in a compressed region produced by cloud collision (Little et al. 1978) or contraction along the predominant magnetic field (Moneti et al. 1984). Quasi-periodic structure (as seen on a larger scale in Fig. 1*a* and on a smaller scale in Fig. 6) could be the result of some magnetohydrodynamic mode (Langer 1978; Carlberg & Pudritz 1991). The distribution of CCS and CS clumps in Figures 1, 7, 8, and 9 suggests that one of these mechanisms is present, especially given their low mass. As noted above, the turbulent velocity dispersion is small ($\lesssim$0.05 km s$^{-1}$) compared to the thermal velocity dispersion of a 10 K gas with mean molecular mass of 2.3 amu. We have searched for velocity gradients in our data and find that the rotation is small, $\lesssim$0.05 km s$^{-1}$ arcmin$^{-1}$ (1.25 km s$^{-1}$ pc$^{-1}$), and makes negligible contribution to support.

What are these clumps in TMC-1 core D? Do they represent localized regions of density, or chemical inhomogeneities, or both? Since the mass estimated for the smaller clumps with a density $\sim 10^5$–$10^6$ cm$^{-3}$ is much less than their virial mass, these clumps are not gravitationally bound. Because TMC-1 appears to be unusual in chemistry and structure, it might seem that conclusions about this source cannot be applied to low-mass star-forming regions in general. However, the properties of the clumps in TMC-1 core D are similar to the properties of the quiescent core in L1498 (Lemme et al. 1995; Velusamy, Kuiper, & Langer 1995). Lemme et al. found from high-resolution $C^{18}O$ and CS observations that L1498 consists of a large bound core with very narrow line widths, 0.11–0.18 km s$^{-1}$, with mass $\sim 1\ M_\odot$. This core is in virial equilibrium and is thermally supported. Their $C^{18}O$ (2–1) data also showed many small sub–solar mass, gravitationally unbound clumps, with narrow line features, similar to the features we extract from our CCS maps of TMC-1. Interferometer observations in CS also show the presence of $<$0.01 pc small-scale structures in the L1498 core (Velusamy et al. 1995). The presence of such structures in both clouds raises some interesting questions about their formation. The more complex structure of TMC-1 may be a collection of objects similar to the L1498 core.

From the number of features in the maps using different density tracers and at different spatial resolution, there appears to be a hierarchy of fragments with an increasing number of features at smaller scales embedded in the larger scale features. While our maps are limited to core D, it appears that the number of features continues to increase at smaller scales at least down to 0.007 pc. Indeed, we see more small-scale features per unit area than do Pound & Blitz (1995), who used different tracers to search for low-mass objects in star-forming regions Oph B and B18. However, we find no evidence for proto–brown dwarfs (bound structures with mass $<0.08\ M_\odot$) similar to the conclusions of Pound & Blitz (1993, 1995). We need more observations to say whether the number distribution turns over at very low mass ($<0.1\ M_\odot$).

We believe that the small sub–solar mass objects seen in TMC-1 core D are an important part of the protostar formation process because of the possibility of coalescence. It has been suggested that fragmentation by thermal instabilities and coalescence of small fragments are important in the formation of stars in the interstellar medium (Murray et al. 1993). Silk (1995) suggest that low-mass fragments grow by coalescence (through collisions) and are likely to form stars with low mass, $\sim$0.2 or 0.3 $M_\odot$. The timescale for dissipation of our CCS fragments (size/sound speed) is $\sim 10^5$ yr for a 20″ feature. Most of the small-scale fragments ($\lesssim$40″) will dissipate because the sound crossing time is somewhat less than the collision time of a few $\times\ 10^5$ yr (depending on the size and assumed velocity dispersion *among* the fragments). However, a fraction of these fragments will collide and perhaps coalesce to form denser bound structures. Because many of the fragments with size 20″ to 45″ are within a factor 2–3 of having sufficient mass to be bound, it would not take more than one or two coalescing collisions to form a bound structure. On the other hand, the smallest features detected in our maps, size $\sim$10″, are so far from being bound (in terms of gravitational mass) that they almost certainly dissipate before colliding with other similar fragments unless they are pressure confined. The sound speed of $\sim$0.2 km s$^{-1}$ for these features suggests that they are transient with lifetimes $<5 \times 10^4$ yr. However, if they are long lived they must be pressure confined.

It is possible that the small clumps are confined by turbulent pressure, since they are embedded (along the axis of the filament) in a more turbulent (velocity width $\sim$1 km s$^{-1}$) lower density gas as traced by $C^{18}O$ (Fig. 2) and $^{13}CO$, perhaps with some additional magnetic contribution as well (e.g., Bertoldi & McKee 1992). Thus, they could have longer lifetimes than estimated here and may have more time to coalesce.

The low masses of the fragments raise another interesting question: do they represent a population of proto–brown dwarfs? Pound & Blitz (1995) claim to see a cutoff in the number of bound clump masses below 0.1 $M_\odot$ in the star-

forming regions Ophiuchus and B18. Although we find that low-mass clumps are more prevalent in a quiescent region than Pound & Blitz, they are all unbound and hence would not form proto–brown dwarfs without some collisional process.

## 6. SUMMARY

We have made a study of the structure of TMC-1 and in particular of core D on scales ranging from 6″ up to 30′ using single-dish and interferometric maps of $C^{18}O$, CCS, and CS. Our $C^{18}O$ map shows hierarchical fragmentation with dense cores embedded in larger elliptical features which are part of a long filamentary, or cylindrical, structure. From the CCS single-dish and interferometric maps we find evidence for many more small-scale structures in individual cores in TMC-1 than previously suspected. The high spectral and spatial CCS maps of TMC-1 show that core D is highly fragmented with structures ranging in size from 10″ to 90″. These fragments have very narrow intrinsic line widths $\lesssim 0.11$–$0.20$ km s$^{-1}$, not much larger than the thermal line width for CCS (0.09 km s$^{-1}$ at 10 K). These narrow line widths indicate that $H_2$ thermal pressure is the dominant support in these fragments and that turbulence and rotation are not significant. The mass of these fragments ranges from $\lesssim 0.01$–$0.15$ $M_\odot$, as estimated from density and volume.

The structure of TMC-1 can be described as hierarchical from large to extremely small scale size roughly over 2 orders of magnitude consisting of (i) long filaments of size $>0.5$ pc and mass of several $M_\odot$; (ii) several cores (which are gravitationally bound) of size $\sim 0.1$ pc and masses 0.5–3 $M_\odot$ distributed along the filament; (iii) cores containing several clumps of size $\sim 0.04$ pc and mass $\sim 0.1$ $M_\odot$ which are mainly gravitationally unbound; and, (iv) clumps containing smaller fragments of size $\sim 0.01$ pc and mass $\sim 0.01$ $M_\odot$, which are almost certainly unbound. The small-scale structures appear to be gravitationally unbound which suggests that fragmentation mechanisms other than a pure Jeans gravitational instability may be important in cold dense cores, or that external pressure confinement is important.

We thank the DSN Goldstone staff for help in operating the 70 m and 34 m antennas and the WBSA, staffs of the NRAO VLA and the OVRO-MMA for assistance in the interferometer observations, G. Wright and R. W. Wilson for help with the $C^{18}O$ map. A. Fuente, P. F. Goldsmith, and D. Wolkovitch kindly provided information on CCS collision rates, and H. Pickett advised us regarding the atomic and line properties of CCS. S. Gulkis and M. Klein have encouraged and supported our work with the DSM antennas. This research was conducted while T. V. held a National Research Council Senior Research Associateship while on leave from the Tata Institute. This research was performed at the Jet Propulsion Laboratory, California Institute of Technology, under contract with the National Aeronautical and Space Administration. The OVRO millimeter array is supported by NSF grant AST 93-14079, the K. T. and E. L. Norris Foundation, and the JPL Directors Discretionary Fund.

## REFERENCES

Benson, P. J., & Myers, P. C. 1989, ApJS, 71, 89
Bertoldi, F., & McKee, C. F. 1992, ApJ, 395, 140
Carlberg, R. G., & Pudritz, R. E. 1991, MNRAS, 247, 353
Duvert, G., Cernicharo, J., & Baudry, A. 1986, A&A, 164, 349
Falgarone, E., Phillips, T. G., & Walker, C. K. 1991, ApJ, 378, 186
Frerking, M. A., Langer, W. D., & Wilson, R. W. 1982, ApJ, 262, 590
Fuente, A., Cernicharo, J., Barcia, A., & Gómez-González, J. 1990, A&A 231, 151
Fuller, G. A., & Myers, P. C. 1992, ApJ, 384, 523.
———. 1993, ApJ, 418, 273
Goodman, A. A., Benson, P. J., Fuller, G. A., & Myers, P. C. 1993, ApJ, 406, 528
Guélin, M., Langer, W. D., & Wilson, R. W. 1982, A&A, 107, 107
Henriksen, R. N., & Turner, B. E. 1984, ApJ, 287, 200
Hirahara, Y., Suzuki, H., Yamamoto, S., Kawaguchi, K., Kaifu, N., Ohishi, M., Takano, S., Ishikawa, S., & Masuda, A. 1992, ApJ, 394, 539
Houlahan, P., & Scalo, J. 1992, ApJ, 393, 172
Hoyle, F. 1953, ApJ, 118, 513
Kitamura, Y., Sunada, K., Hayashi, M., & Hasegawa, T. 1993, ApJ, 413, 221
Kroto, H., Kirby, C., Walton, D. R. M., Avery, L. W., Broten, N. W., MacLeod, J. M., & Oka, T. 1978, ApJ, 219, L133
Langer, W. D. 1978, ApJ, 225, 95
Langer, W. D., Glassgold, A. E., & Wilson, R. W. 1987, ApJ, 322, 450
Langer, W. D., Wilson, R. W., & Anderson, C. H. 1993, ApJ, 408, L45
Larson, R. R. 1981, MNRAS, 194, 809
Lemme, C., Walmsley, C. M., Wilson, T. L., & Muders, D. 1995, A&A, in press
Little, L. T., Macdonald, G. H., Riley, P. W., & Matheson, D. N. 1978, MNRAS, 183, 805
MacLaren, I., Richardson, K. M., & Wolfendale, A. W. 1988, ApJ, 333, 821
Miesch, M. S., & Bally, J. 1994, ApJ, 429, 645
Monaghan, J. J., & Lattanzio, J. C. 1991, ApJ, 375, 177
Moneti, A., Pipher, J. I., Helfe, H. L., McMillan, R. S., & Perry, M. L. 1984, ApJ, 282, 508
Murray, S. D., White, S. D. M., Blondin, J. M., & Lin, D. N. C. 1993, ApJ, 407, 588
Myers, P. C., & Benson, P. J. 1983, ApJ, 266, 309
Myers, P. C., & Fuller, G. A. 1992, ApJ, 396, 631
Myers, P. C., Fuller, G. A., Goodman, A. A., & Benson, P. J. 1991, ApJ, 376, 561
Nakano, T. 1984, Fundam. Cosmic Phys., 9, 139
Olano, C. A., Walmsley, C. M., & Wilson, T. L. 1988, A&A, 196, 194
Pickett, H. H., Poynter, R., & Cohen, E. 1991, Submillimeter, Millimeter and Microwave Line Catalog 3e (JPL Tech. Rep. 80-23)
Pound, M. W., Bania, T. M., & Wilson, R. W. 1990, ApJ, 351, 165
Pound, M. W., & Blitz, L. 1993, ApJ, 418, 328
———. 1995, ApJ, 444, 270
Quirk, M. P., Wilk, M. F., Garyantes, M. F., & Grimm, M. J. 1988, IEEE Trans. on Acoustics, Speech & Signal Processing, 36, 1854
Saito, S., Kawaguchi, K., Yamamoto, S., Ohishi, M., Suzuki, H., & Kaifu, N. 1987, ApJ, 317, L115
Silk, J. 1995, ApJ, 438, L41
Schloerb, F. P., & Snell, R. L. 1984, ApJ, 283, 129
Snell, R. L., Langer, W. D., & Frerking, M. A. 1982, ApJ, 255, 149
Spitzer, L., Jr. 1968, Diffuse Matter in Space (New York: Interscience)
Stutzki, J., & Gusten, R. 1990, ApJ, 356, 513
Suzuki, H., Yamamoto, S., Ohishi, M., Kaifu, N., Ishikawa, S., Hirahara, Y., Takano, S., & Masuda, A. 1992, ApJ, 392, 551
Tatematsu, K., et al. 1993, ApJ, 404, 643
Tölle, F., Ungerechts, H., Walmsley, C. M., Winnewisser, G., & Churchwell, E. 1981, A&A, 95, 143
Velusamy, T., Kuiper, T. B. H., & Langer, W. D. 1995, in preparation
Velusamy, T., Kuiper, T. B. H., Langer, W. D., Levin, S., & Olsen, E. T. 1993, in The Physics and Chemistry of Molecular Clouds, Second Zermatt Symposium, ed. J. Stutzki & G. Winnewisser, in press
Williams, J. P., de Geus, E., & Blitz, L. 1994, A&A, 428, 693
Wolkovitch, D., Goldsmith, P. F., Langer, W. D., Kuiper, T. B. H., Heyer, M., Velusamy, T., & Levin, S. 1995, in preparation